



**HAL**  
open science

# Multi-dimensional morphology of hydride diffusion layer and associated sequential twinning in commercial pure titanium

Qian Wang, Shun Xu, Yajun Zhao, Jean-Sébastien Lecomte, Christophe Schuman

► **To cite this version:**

Qian Wang, Shun Xu, Yajun Zhao, Jean-Sébastien Lecomte, Christophe Schuman. Multi-dimensional morphology of hydride diffusion layer and associated sequential twinning in commercial pure titanium. *Journal of Materials Science and Technology*, 2021, 103, pp.105-112. 10.1016/j.jmst.2021.07.010 . hal-03863823

**HAL Id: hal-03863823**

**<https://cnrs.hal.science/hal-03863823>**

Submitted on 22 Nov 2022

**HAL** is a multi-disciplinary open access archive for the deposit and dissemination of scientific research documents, whether they are published or not. The documents may come from teaching and research institutions in France or abroad, or from public or private research centers.

L'archive ouverte pluridisciplinaire **HAL**, est destinée au dépôt et à la diffusion de documents scientifiques de niveau recherche, publiés ou non, émanant des établissements d'enseignement et de recherche français ou étrangers, des laboratoires publics ou privés.

1           **Multi-dimensional morphology of hydride diffusion layer and associated**  
2                           **sequential twinning in commercial pure titanium**

3           Qian Wang <sup>a,b</sup>, Shun Xu <sup>c</sup> Yajun Zhao <sup>d,\*</sup>, Jean-Sébastien Lecomte <sup>a,b,\*</sup>, Christophe Schuman <sup>a,b,\*</sup>

4           <sup>a</sup> Laboratoire d'Etude des Microstructures et de Mécanique des Matériaux (LEM3), Université de Lorraine  
5           CNRS, Arts et Métiers ParisTech, Metz , 57073, France

6           <sup>b</sup> Laboratory of Excellence on Design of Alloy Metals for low-mAss Structures (DAMAS), University of  
7           Lorraine, 57073, France

8           <sup>c</sup> School of Iron and Steel, Soochow University, Suzhou, 215021, China.

9           <sup>d</sup> School of Materials Science and Engineering, Dalian Jiaotong University, Dalian, 116021, China

10          \*Corresponding author.

11          E-mail adresses: [yajunzhao@djtu.edu.cn](mailto:yajunzhao@djtu.edu.cn)

12                           [jean-sebastien.lecomte@univ-lorraine.fr](mailto:jean-sebastien.lecomte@univ-lorraine.fr)

13                           [christophe.schuman@univ-lorraine.fr](mailto:christophe.schuman@univ-lorraine.fr)

14          **Abstract**

15          The dominant hydride precipitates have been well demonstrated to follow two types  
16          of orientation relationships (ORs) with Ti matrix: OR1 with  $\{0001\} // \{1\bar{1}1\}$  ,  
17           $\langle 1\bar{2}10 \rangle // \langle 110 \rangle$  , and OR2 with  $\{0001\} // \{001\}$  ,  $\langle 1\bar{2}10 \rangle // \langle 110 \rangle$  . Our previous work  
18          reveals the orientation dependence of the hydride nucleation with above two ORs. Within  
19          the grains with special orientations, the complicated interactions of different variants  
20          inside Ti-hydride diffusion layer are further characterized in this work. The orientations  
21          favorable for OR1 hydride layer are:  $\{10\bar{1}3\}$  plane parallel to sample surface  
22          corresponding to the layer with one OR1 variant dominated and *c*-axis parallel to the  
23          surface normal with multiple OR1 variant layer preferred. As for OR2 hydride layer, the  
24          orientation of  $\{10\bar{1}0\}$  plane parallel to the sample surface is favorable for three  
25          symmetrical OR2 variants, while *a*-axis parallel to the normal direction prefers two  
26          preferential OR2 variants. Furthermore,  $\{10\bar{1}2\}$  extension twins and  $\{11\bar{2}2\}$  contraction

1 twins are activated to accommodate the hydride-induced surface expansion and local  
2 misfit strain associated with the formation of OR1 hydride. The stimulation of these two  
3 twins is also orientation dependent:  $\{10\bar{1}2\}$  and  $\{11\bar{2}2\}$  twins can effectively  
4 accommodate the surface expansion of grains with *c*-axis parallel to and deviated from  
5 the surface normal of the sample, respectively. The further variant selection for each twin  
6 mode is performed through shear accommodation of hydride-twin pairs.

7

8 **Keywords:** Titanium; Hydride; Cross section; Twin; Variant selection;

9

## 1 **1. Introduction**

2 The combination of high corrosion resistance, strength-to-weight ratio, and  
3 exceptional biocompatibility of titanium and its alloys allows widespread applications  
4 especially in aerospace and biomedical industries[1]. When subjected to hydrogen-rich  
5 service conditions, nevertheless, the formation and transformation of hydride  
6 precipitations in Ti would induce high internal stress in the alloys, which is regarded as  
7 the origin of several important alloy properties decrease, such as ductility and toughness  
8 [2]. Indeed, the solubility of H in titanium is low, 0.15 wt. % in  $\alpha$ -Ti at 300 °C [3], the  
9 consensus is that, even a small quantity of hydrogen will cause the formation of  $\text{TiH}_x$   
10 hydrides in Ti and produce a considerable drop in alloy properties [4]. Accordingly,  
11 hydride precipitation has been considered as a major barrier for reliable applications of  
12 Ti alloys under hydrogen-rich conditions.

13 The phase structures of hydrides formed in Ti at room temperature are determined by  
14 hydrogen concentration: TiH with face-centered tetragonal (FCT) structure forms at  
15 relative low hydrogen concentration and transforms into the face-centered cubic (FCC)  
16  $\text{TiH}_x$  (with x ranging between 1.5 and 2). The FCC phase ( $\delta$  phase) is the most stable and  
17 prevalent hydride in titanium, which changes its lattice structure and transforms into the  
18 FCT  $\text{TiH}_2$  with further increase of hydrogen concentration [5–9]. Another key factor that  
19 dominates the formation of hydride precipitations in titanium is crystallographic  
20 orientation. Four types of orientation relationships between the hexagonal close packed  
21 (HCP) Ti matrix and  $\delta$  hydrides (FCC structured) have been reported in Refs [5–8], as  
22 shown in Table 1. OR1 (with  $\{0001\} // \{1\bar{1}1\}$  ,  $\langle 1\bar{2}10 \rangle // \langle 110 \rangle$  ) and OR2  
23 ( $\{0001\} // \{001\}$  ,  $\langle 1\bar{2}10 \rangle // \langle 110 \rangle$ ) were the most common orientation relationships in  
24 pure titanium and referred to as B-type and P-type ORs respectively, according to their

1 nucleation mechanism [10]. While OR3 ( $\{10\bar{1}0\} // \{1\bar{1}1\}$ ,  $\langle 1\bar{2}10 \rangle // \langle 110 \rangle$ ) and OR4  
2 ( $\{\bar{1}011\} // \{001\}$ ,  $\langle 1\bar{2}10 \rangle // \langle 110 \rangle$ ) were rarely observed, which were firstly reported in [5].

3 In our previous work [10], orientation dependence of hydride precipitation in  
4 commercially pure titanium has been investigated in detail. The formation of hydrides  
5 is significantly dependent on the matrix orientation for the reason of strain  
6 accommodation. The most favorable grain orientations for OR1 and OR2 hydride  
7 transformation are with  $\{10\bar{1}3\}$  and  $\{10\bar{1}0\}$  interface planes parallel to the diffusion  
8 surface, as the largest misfit strains along their interface plane normal can be  
9 accommodated by free surface relaxation. Besides, the interaction between hydride  
10 variants can also play a supportive role in accommodating the phase transformation-  
11 induced strain. OR1 hydride packets were observed under electron backscattered  
12 diffraction (EBSD) characterization in [11], the hydride grains inside the packet are in  
13  $\{111\} \langle 11\bar{2} \rangle$  twin relationships to relax the anisotropic misfit strain of hydride  
14 transformation. Conforto and Caillard [8] proposed that the hydride precipitates in  
15 different ORs prefer to form clusters to realize a more isotropic distribution of misfit  
16 strain produced by hydride transformation and decrease the total stored elastic energy.  
17 Indeed, hydride clusters formed by OR1 and OR2 hydrides were observed in [10], which  
18 can be energy favorable to accommodate the nearly perpendicular misfit strain of these  
19 two ORs transformation. However, the research efforts of [10] on orientation dependence  
20 and the interactions of hydride variants formed by electrolytic hydrogen charging were  
21 only carried out on 2D sample surface. Technically, a certain time of electropolishing on  
22 the post-charged sample surface is always necessary to achieve EBSD phase  
23 identification, that will inevitably, erase some valuable information of hydride diffusion

1 layer. It is therefore essential to conduct further investigations on the section  
2 microstructure of hydride layer.

3 Owing to the large volume expansion of hydride transformation, dislocations are  
4 necessary to accommodate the dilatation misfit between hydride and hexagonal matrix.  
5 Carpenter [12] suggested that OR1 hydrides are formed by the dissociation of the normal  
6  $1/3 \langle 1\bar{2}10 \rangle$  dislocations. Around the top and bottom ends of the hydride precipitate, shear  
7 loop dislocations on the basal plane with  $\mathbf{b} = 1/3 \langle 1\bar{2}10 \rangle$  are punched out and extending  
8 in the direction of their Burgers vectors [7]. The formation of OR2 hydrides is related to  
9 a ledge mechanism [6], including a shear component in  $\langle 1\bar{2}10 \rangle$  and the normal dilatation  
10 component in  $\langle 10\bar{1}0 \rangle$  caused by volume variation. Conforto and Caillard [5] proposed  
11 that the transition of OR2 produces two opposite prismatic loops along the interface,  
12 contributing to the relaxation of misfit in the  $\langle 1\bar{2}10 \rangle$  direction. Up to now, detailed study  
13 on the formation mechanism and misfit dislocations related to the OR3 and OR4 hydrides  
14 have not been reported. In addition, twins were also observed together with OR1 hydride  
15 precipitates [10,11], but the hydride-twin accommodation mechanism is still not well  
16 understood.

17 In the present work, multi-dimensional characterization of hydride layer in  
18 commercial pure Ti (CP-Ti) formed by electrolytic hydrogen charging was performed.  
19 The anisotropic section microstructure of hydride diffusion layer was examined in detail  
20 for the first time via EBSD measurements, driving a further in-depth study on the  
21 orientation dependence of hydride interaction. The associated plastic behaviors induced  
22 by hydride transformation and corresponding accommodation mechanism were also  
23 investigated.

## 24 **2. Methodology**

1       Commercially pure Ti rolled sheets (T40, ASTM grade 2) with thickness of 1.5 mm  
2 were used in the present work. The as-received sheets were firstly annealed in vacuum  
3 condition at 800 °C for 3 h to obtain a fully recrystallized microstructure with an average  
4 grain size of ~50 μm. The texture is a typical split basal texture with basal pole oriented  
5 ± 20 ° away from normal direction (**ND**) of the sheet towards transverse direction (**TD**).  
6 Hydrogen charging was performed for the specimens by employing an electrolytic  
7 method [10] in an electrolyte consisting of 1/3 volume phosphoric acid and 2/3 volume  
8 glycerin under an applied current density of 2 kA/m<sup>2</sup>. Sample was charged for 168 h to  
9 obtain stable δ-hydride (FCC) diffusion layer with a hydrogen concentration of 123 wt  
10 ppm, which is the same as that in [10].

11       Two sets of samples are prepared to observe the section microstructure of hydride  
12 diffusion layer (Sample A, Fig. 1a) and hydride-induced plastic deformation (Sample B,  
13 Fig. 1b). In order to examine the anisotropic section microstructures of OR1 and OR2  
14 hydride diffusion layers, both the transverse direction (**TD**) and rolling direction (**RD**)  
15 surfaces of Sample A were ground with SiC papers of grits to 2000<sup>#</sup> and then charged as  
16 diffusion surface. The textures of **TD** and **RD** surfaces are favorable for respective OR1  
17 and OR2 hydride transformations [10]. The hydrogenated sample were mounted with  
18 Struers Polyfast resin to protect the diffusion surface during the metallographic  
19 preparation process. After ground and chemical-mechanical polished with OPS (Struers),  
20 the diffusion layer section on **ND** surface was embellished by argon ion polishing using  
21 Gatan PECS II apparatus with 5kV for 2h. For the characterization of hydride nucleation  
22 inside hydride layer (Sample B), **ND** surface was chosen as the diffusion surface. The  
23 ground sample was hydrogen charged and then electrolytic polished at 5 °C for 1 s with  
24 voltage of 30 V in a solution of 10 vol% perchloric acid in methanol.

1        Microstructure characterization was performed through an interrupted in-situ method  
2 using a tungsten thermionic emission Jeol-6490 and field emission gun Jeol-6500F  
3 scanning electron microscopy (SEM), that are both equipped with EBSD detector and  
4 AZtec software package (Oxford Instruments) for data acquisition. To balance the  
5 characterization accuracy and efficiency, Jeol-6490 was used for high speed EBSD  
6 detection with the purpose of obtaining enough statistical information in large areas,  
7 while Jeol-6500F was employed to acquire detailed examination.

### 8    **3. Results**

#### 9    **3.1 Multi-dimensional morphology of hydride diffusion layer**

10        The SEI – Secondary Electron Image showing the section microstructure of the  
11 hydride layer is presented in Fig. 2a. It can be seen that the sample and the resin are  
12 bonded tightly, with a stress-free area at the junction (the area between red dotted lines),  
13 which is ion polishing area obtainable under EBSD measurement. The higher-  
14 magnification SEI for the black box area in Fig. 2a is shown in Fig. 2b. In which, the  
15 interface between Ti matrix and hydride layer in light gray curve can be observed more  
16 clearly, highlighted by yellow dotted line. The thickness of hydride layer can be therefore  
17 measured around 7  $\mu\text{m}$ . Besides, the section structures formed on **TD** or **RD** diffusion  
18 surface are indistinguishable under SEI.

19        Fig. 2c and d present the **TD**-IPF and **RD**-IPF maps of section microstructures of  
20 diffusion layers formed on respective **TD** and **RD** surfaces, that are colored by hydrogen  
21 diffusion directions. The IPF maps include two regions: FCC hydride layer (upper side)  
22 and HCP titanium matrix (lower side). It is obvious that the hydride layer has much lower  
23 indexing rates, especially at the junction area near titanium matrix, where Kikuchi  
24 patterns are too blur to be detected due to the large lattice distortion induced by hydride

1 transformation. Inside hydride layer, the hydride microstructures are dependent on the  
2 grain orientations of Ti matrix. According to Fig. 2c and d, some grains form  
3 homogeneous hydride layers with almost unique hydride variant, and some hydride layers  
4 contain complicated hydride interactions. Although with various hydride microstructures,  
5 the hydride layers are continuous and similar in thickness, as well as the hydride–matrix  
6 interfaces are approximately parallel to the diffusion surface.

7 The orientation dependent hydride nucleation on the diffusion surface has been  
8 investigated in our former work [10]. However, some valuable information inside hydride  
9 layer was lost when the surface prepared by electrolytic polishing. In this work, the  
10 anisotropic section microstructures of hydride layers are further investigated. According  
11 to the results in [10], there appear four typical titanium matrix orientations with multiple  
12 hydride platelet microstructures: (1)  $\{10\bar{1}3\}$  planes parallel to the diffusion surface are  
13 favorable for the nucleation of single OR1 hydride variant; (2)  $c$ -axis oriented along  
14 diffusion direction prefers multiple OR1 variants; (3)  $\{10\bar{1}0\}$  planes aligned to the  
15 diffusion surface refer to one dominant OR2 hydride variant; (4) OR1-OR2 hydride  
16 clusters are formed in the grain with  $a$ -axis along diffusion direction. In the present  
17 research, the section microstructures of hydride layers in the grains (G1-G4)  
18 corresponding to the above four typical orientations are characterized, as shown in Fig. 3.  
19 G1 and G2 (Fig. 3a and b) with dominant OR1 hydride layer are selected from **TD**  
20 diffusion surface (Fig. 2c), while G3 and G4 (in Fig. 3c and d) preferring OR2 hydride  
21 transformation are from **RD** surface (Fig. 2d). Interestingly, according to Fig. 3, no matter  
22 which type of grain orientation, more than one hydride variant is activated inside hydride  
23 layer. For convenience,  $B_i$  and  $P_j$  are employed to denote the six OR1 and three OR2  
24 hydride variants ( $i=1,2,3\dots6$  and  $j=1,2,3$ ) as listed in Table 2. The OR1 hydride variants

1 are defined by the interface planes with corresponding shear of Shockley dislocation,  
2 while OR2 hydrides were defined by only interface planes. The different expression for  
3 OR1 and OR2 variants are determined by their transformation mechanism, which will be  
4 discussed in Section 4.1.

5 As mentioned above, the orientation of G1 ( $\{10\bar{1}3\}$  interface plane parallel to  
6 diffusion surface is favorable for single OR1 hydride variant reported in [10]. Indeed, a  
7 major variant ( $B_4$ ) almost occupy entire hydride layer in Fig. 3a. According to the pole  
8 figures, the  $(\bar{1}013)$  interface plane of dominant  $B_4$  is the closest to **TD** surface. This  
9 accords with the investigation of variant selection reported in [10], the hydride variant  
10 with its interface closest parallel to diffusion surface is selected because of its highest  
11 capacity to accommodate the misfit distortion through free surface. However, inside  
12 hydride layer, other hydride variants are also activated likely by the accumulated misfit  
13 strain of  $B_4$ . Some  $B_5$  variants with  $(0\bar{1}13)$  interface slightly deviated from **TD** surface  
14 precipitate near the diffusion surface and embed into  $B_4$  hydride layer. A few small OR2  
15 particles are induced at the matrix-hydride junction, because the orientation of G1 is  
16 relatively unfavorable for OR2 transformation. It should be noticed that some OR3  
17 hydrides appear along the upside sample edge. Normally, OR3 transformation is difficult  
18 in  $\alpha$ -Ti matrix because of large misfit (around 15%) along  $c$ -axis, while the high density  
19 of dislocations on the free surface provides the possibility for the nucleation of OR3  
20 hydrides.

21 Grain 2 has the orientation of  $c$ -axis close to **TD** (diffusion direction) preferring  
22 multiple OR1 variants. In Fig. 3b, four OR1 variants ( $B_1$ ,  $B_3$ ,  $B_4$  and  $B_6$ ) are formed inside  
23 hydride layer. According to the pole figures,  $B_1$  and  $B_6$  are the most favorable two variants  
24 and thus occupy a large proportion of hydride layer, while  $B_3$  and  $B_4$  are less favorable

1 processing lamellar shape. Noting that,  $B_1$ - $B_4$  and  $B_3$ - $B_6$  usually occur in pairs. The  
2 dislocation accumulation produced by the formation of  $B_6$  and  $B_1$  would induce the  
3 formation of  $B_3$  and  $B_4$  respectively, due to the fact that the Shockley dislocations are  
4 along opposite directions between  $B_i$  and  $B_{i+3}$ . The large distortion produced by the  
5 interactions of different variants results in a thicker non-indexed area at the hydride-  
6 matrix junction than G1. Besides, as investigated in the next section,  $\{10\bar{1}2\}$  twins are  
7 always stimulated at the OR1 hydride interface in the grain with G2 orientation, but rarely  
8 detected on the cross section.

9 [Fig. 3c](#) shows the hydride layer in G3 with the orientation of  $\{10\bar{1}0\}$  parallel to the  
10 **RD** surface (diffusion surface). Unlike the result in [\[10\]](#) that one dominant OR2 variant  
11 was activated, all the three OR2 hydride variants happen and interact in G3. Thus, the  
12 hydride layer in OR2 favorable grain is different from OR1 favorable grain dominated by  
13 the most favorable hydride variant, for an example  $B_4$  in G1 ([Fig. 3a](#)). As shown in [Fig.](#)  
14 [3c](#), in addition to the most favorable variant  $P_1$ , both  $P_2$  and  $P_3$  variants with their  $\{10\bar{1}0\}$   
15 interfaces  $\sim 60^\circ$  away from **RD** surface are also formed. The together nucleation of three  
16 symmetric OR2 hydride variants can be induced by the extremely anisotropic lattice  
17 dilatation of OR2 transformation:  $-6.0\%$  along  $\langle 0001 \rangle$ ,  $+5.5\%$  along  $\langle \bar{1}2\bar{1}0 \rangle$  and  $+21.8\%$   
18 along  $\langle 10\bar{1}0 \rangle$  [\[10\]](#). During hydrogen diffusion,  $P_1$  preferentially precipitates near the  
19 sample surface, partial misfit strain along  $[10\bar{1}0]$  can be relaxed through free surface.  
20 Subsequently, symmetric  $P_2$  and  $P_3$  are formed interconnecting with  $P_1$  to realize isotropic  
21 misfit strain inside hydride layer. In addition, a few OR1 hydrides are also activated inside  
22 the diffusion layer and/or at the hydride-matrix junction. Conforto and Caillard [\[8\]](#)  
23 suggested that, due to the nearly perpendicular misfit strain direction, the interconnection  
24 between OR1 and OR2 hydrides can decrease the total stored elastic energy.

1 G4 represents the grain with  $\langle \bar{1}2\bar{1}0 \rangle$  parallel to the hydrogen diffusion direction (**RD**),  
2 that hydrides nucleate in OR1-OR2 clusters [10]. However, in Fig. 3d, the majority of  
3 hydride layer is OR2 hydride indicating that G4 is also more favorable for OR2 than OR1  
4 transformation. P<sub>1</sub> and P<sub>3</sub> variants are the relatively major components of hydride layer,  
5 as well as a small amount of P<sub>2</sub> variants occur at the junction of hydride layer and Ti  
6 matrix. According to the pole figures (Fig. 3d), P<sub>2</sub> variant is extremely unfavorable,  
7 presenting a large deviation  $\sim 90^\circ$  of its (01 $\bar{1}$ 0) pole from the pole figure center, thus the  
8 formation of symmetric accommodation between three OR2 variants is restrained in G4.

9 In general, the section microstructure of hydride layer reveals more details of hydride  
10 interaction than the characterization of hydride nucleation in [10]. Among OR1-OR3  
11 transformation, OR1 is determined in all the four typical grains, and thus the most likely  
12 to happen. While OR2 hydride did not precipitate in G2 indicating that *c*-axis parallel to  
13 diffusion direction is extremely unfavorable orientation for OR2 transformation. OR3  
14 transformation is the most difficult, because it is only activated on the surface of OR1  
15 hydride layer in G1. It can be speculated that the pre-existing OR1 hydrides play an  
16 important role on OR3 hydride nucleation, which will be discussed in Section 4.1.

### 17 **3.2 Plastic accommodations stimulated by hydride transformation**

18 Hydride nucleation has already been studied on diffusion surface to investigate the  
19 variant selection in our former work [10], where some micro twins were occasionally  
20 found near hydride platelets. In this section, the plastic deformation induced by hydride  
21 nucleation are further studied. For an explicit study of the hydrides and twins, two EBSD  
22 maps of post-charged surface are drawn: ND-IPF map (Fig. 4a) and phase map (Ti: silver,  
23 Hydride: white) with colored boundaries (Fig. 4b). The corresponding color definitions  
24 are presented under individual map. In Fig. 4b, the interface planes of OR1 hydrides are

1 colored by blue lines and OR2 hydride interfaces by pink lines. The fraction of OR1  
2 hydrides is much higher than that of OR2 hydrides showing the favorable texture of **ND**  
3 surface for OR1 transformation.

4 Two types of twins are observed: majority of  $\{10\bar{1}2\}$  extension twins (green lines)  
5 and a smaller quantity of  $\{11\bar{2}2\}$  contraction twins (orange lines) as well. Some twins are  
6 activated inside grain matrix, while the others appear specially at the OR1 hydride  
7 interface regarded as hydride-induced twins. Twin variants are studied in detail by  
8 employing the same expression method in [13]:  $T_i^I$  ( $i = 1, 2, \dots, 6$ ) denoted the six  $\{10\bar{1}2\}$   
9 ( $T_i^I$ ) tension twin variants, while the six  $\{11\bar{2}2\}$  twin variants are represented by  $C_i^I$  ( $i =$   
10 1, 2, ...6), as presented in Table 2. Neither  $\{11\bar{2}4\}\langle 22\bar{4}3\rangle$  or  $\{11\bar{2}1\}\langle \bar{1}\bar{1}26\rangle$  twin  
11 appears in our experiments, they are usually activated when titanium is deformed at high  
12 strain rate [14]. Moreover, although no twin is activated, significant orientation change  
13 occurs in the grains with OR2 hydride.

14 To study the hydride-stimulated twinning, the OR1 hydride-twin pairs are examined  
15 in detail. Two specific grains (Grain I and Grain II) containing respective  $\{10\bar{1}2\}$  and  
16  $\{11\bar{2}2\}$  twins are extracted from Fig. 4, their IPF maps (Fig. 5a and e) and corresponding  
17 phase maps (Fig. 5b and f) with the same color definition as Fig. 4 are shown in Fig. 5.  
18 In Fig. 5a and b, relatively large  $\{10\bar{1}2\}$  twins are formed on both sides of OR1 hydride  
19 interfaces. According to the pole figures in Fig. 5c, inside the red circles, the hydride  
20 variant  $B_5$  and twin variant  $T_2^I$  are selected. The  $\{10\bar{1}2\}$  twin orientation existing a large  
21 deviation from OR1 favorable orientation ( $\{10\bar{1}3\}$  plane parallel to diffusion surface),  
22 and restrains further thickening of hydride lamellas. For the grain containing  $\{11\bar{2}2\}$   
23 twins in Fig. 5e and f, smaller  $\{11\bar{2}2\}$  twin plates are observed due to the larger shear

1 necessary for the formation of  $\{11\bar{2}2\}$  twins than  $\{10\bar{1}2\}$  extension twins. The hydride  
2 platelets gradually become thinner or/and break off when  $\{11\bar{2}2\}$  twins are stimulated  
3 near the hydride tips. The growth of intragranular hydrides can be explained via the auto-  
4 catalytic nucleation mechanism [15,16]. The chemical potential wells produced by the  
5 misfit strain at the growth front attract the hydrogen atoms and then control the path for  
6 further nucleation and growth of hydride. However, the local strain can be relaxed by the  
7 activation  $\{10\bar{1}2\}$  or  $\{11\bar{2}2\}$  twins, which decrease the chemical potential wells and also  
8 relative hydrogen affinities. Therefore, when a hydride stimulates the twinning process  
9 or intersects with an impinging twin, further growth will be restrained or changed.

10 The grains containing hydride-twin pairs are selected from Fig. 4, their orientations  
11 are projected into IPFs, as shown in form of IPF contouring maps in Fig. 5d and h, where  
12 the red points represent the most favorable orientations for OR1 and OR2 transformations.  
13 According to Fig. 5d,  $\{10\bar{1}2\}$  twins prefer to be stimulated in the grains with *c*-axis close  
14 to hydrogen diffusion direction (**ND**). The grain with *c*-axis aligned to diffusion direction  
15 involve large distortion produced by complex interactions between multiple hydride  
16 variants, as reported in [10]. Thus, the local stress of hydride interaction can be also  
17 partially relaxed by the stimulation of  $\{10\bar{1}2\}$  twin. For  $\{11\bar{2}2\}$  twins, the grain  
18 orientations locate between the orientations favorable for OR1 and OR2, as shown in Fig.  
19 5h, which prefer unique hydride variant, such as Fig. 5e.  $\{11\bar{2}2\}$  twin-hydride pair is  
20 rarely observed in the grain with more than one hydride variant showing that the hydride  
21 interaction restrains the  $\{11\bar{2}2\}$  twin nucleation. Furthermore, 10 hydride- $\{10\bar{1}2\}$  twin  
22 pairs and 10 hydride- $\{11\bar{2}2\}$  twin pairs are detected on the observe surface of Fig. 4, they  
23 can be described unanimously by  $B_i-T_{i+3}^I$  and  $B_i-C_i^I$ , respectively. The reason for the  
24 orientation dependent twin nucleation and the accommodation mechanism of  $\{10\bar{1}2\}$  and

1  $\{11\bar{2}2\}$  twins on OR1 transformation resulting in the special twin variant selection can  
2 be found in Section 4.2.

3 [Fig. 6a](#) shows the IPF map of a typical grain (Grain III) with OR2 hydride nucleation  
4 at grain boundary. The  $\{10\bar{1}0\}$  interfaces of OR2 hydrides are less straight than the  
5  $\{10\bar{1}3\}$  interfaces of OR1 hydrides. The preferential grain boundary nucleation and  
6 curved interface can relax the large misfit dilatation of OR2 transformation along  $\langle 10\bar{1}0 \rangle$   
7 (about 20%). Furthermore, according to the identified grain boundaries ( $>5^\circ$ , black lines)  
8 inside Grain III, the intragranular orientation changes are more significant in the OR2  
9 favorable grains due to a high density of geometrically necessary dislocation produced  
10 by hydrogen diffusion, which will be the favorable positions for subsequent nucleation of  
11 OR2 hydride in the grain interior.

12 Using the method of Chun et al. [\[17\]](#), IGMA (In-Grain Misorientation Axes) analysis  
13 of EBSD data is performed to explore the activated slip mode. The lower cutoff  
14 misorientation angle in IGMA analysis is taken as  $1.2^\circ$ , because of the limited angular  
15 resolution of the EBSD analysis. Actually, the IGMA distributions of material-point pairs  
16 between  $1.2^\circ$  and  $2^\circ$  is enough to investigate active slip mode, which is plotted for Grain  
17 III as shown in [Fig. 6c](#), showing strong intensities around  $\langle 0001 \rangle$ . By matching the  
18 Taylor axis, such IGMA distributions are attributed to the predominant activation of  
19 prismatic  $\langle a \rangle$  slip. According to Weatherly et al. [\[18\]](#), the HCP-FCC transformation of  
20 OR2 hydrides was formed by the partial dislocations on prismatic plane. Thus, it can be  
21 inferred that the accumulation of prismatic  $\langle a \rangle$  dislocations is produced for the nucleation  
22 of intragranular OR2 hydrides.

## 23 **4. Discussion**

#### 1 4.1 HCP-FCC structure transformation of OR1-OR3 hydrides

2 In addition to the anisotropic lattice misfit strain, the mechanisms of HCP-FCC  
3 structure transformation for OR1 and OR2 hydrides are also different [18], as illustrated  
4 in Fig. 7, which leads to the multiple plastic accommodation modes: twins are commonly  
5 induced by OR1 hydrides (Fig. 5) and prismatic dislocations are found in OR2 favorable  
6 grains (Fig. 6). The HCP-FCC transformation of OR1 hydride is shown in Fig. 7a, a  
7 simple shear introduced by the slip of Shockley dislocation along  $[10\bar{1}0]$  on  $(0001)$  plane  
8 converts the hexagonal lattice (black circle) into cubic structure (blue circle). The angle  
9  $\alpha$  produced by  $\mathbf{b} = 1/3[10\bar{1}0]$  is around  $20.0^\circ$ :

$$\alpha = \arctan\left(\frac{|\mathbf{b}|}{c}\right) = \arctan\frac{a}{\sqrt{3}c} \quad (1)$$

10 where  $a = 0.295$  nm and  $c = 0.468$  nm are the lattice parameters of  $\alpha$ -Ti. The OR1 hydride  
11 will be formed by the HCP-FCC transformation combined with lattice dilatation, of which  
12 the energy favorable habit plane  $\{10\bar{1}3\}$  is around  $31^\circ$  from  $(0001)$  shear plane.  
13 Dislocations and/or twins are required to accommodate the shear and lattice misfit of  
14 hydride transformation.

15 As for OR2 hydride transformation, there also exists a shear of  $30^\circ$  along  $[1\bar{2}10]$  on  
16 prismatic plane in Fig. 7b produced by prismatic partial dislocations, which bring the  
17 hexagonal atoms into face-centered arrangement [18]. Besides, atom rearrangements  
18 (shuffles) are needed along the  $[10\bar{1}0]$  invariant plane normal. Prismatic dislocations are  
19 attributed to the originating of HCP-FCC structure transformation of OR2 hydride, which  
20 is consistent with our experimental results in Fig. 6. Furthermore, a sample shear  
21 deformation is always accompanied by a rigid body rotation, which should destroy the  
22 undistorted  $\{10\bar{1}0\}$  interface plane. Internal deformation mechanisms (like slip, twinning

1 or shuffling) are necessary to accommodate the shear on  $\{10\bar{1}0\}$  plane and achieve the  
2 experimental orientation relationship of OR2. Indeed, internal twins and dislocations  
3 were observed by TEM at hydride-matrix interfaces [18], but not detected by EBSD  
4 measurement in our work.

5 The activation of OR3 transformation is hard in  $\alpha$ -Ti due to the large misfit strain  
6 along  $c$ -axis, while it was observed at the edge of OR1 hydride layer, as mentioned before  
7 in Fig. 3a. It was speculated that the surface defects and B<sub>4</sub> hydride layer can stimulate  
8 the OR3 hydride nucleation. The activated B<sub>4</sub> and OR3 variants have respective habit  
9 planes of  $(\bar{1}013)//(1\bar{1}0)$  and  $(\bar{1}010)//(\bar{1}11)$  with the same zone axis  $\langle\bar{1}2\bar{1}0\rangle//\langle\bar{1}\bar{1}0\rangle$ . Their  
10 HCP-FCC transformations are illustrated in Fig. 8, where the black to blue refers to OR1  
11 and black to red represents OR3 transformation. If not considering lattice dilatation, the  
12 difference between FCC structures of OR1 and OR3 hydrides is only a simple lattice  
13 rotation  $\sim 20.0^\circ$  around  $\langle\bar{1}2\bar{1}0\rangle//\langle\bar{1}\bar{1}0\rangle$  (the same as  $\alpha$  in Fig. 7a). Thus, it could be  
14 derived that the OR3 precipitates are induced from the pre-existing OR1 variant B<sub>4</sub> to  
15 accommodate the accumulated distortion inside hydride layer. Indeed, the experimental  
16 misorientation between them is  $\sim 26.6^\circ/\langle\bar{1}\bar{1}0\rangle$ . The deviation of misorientation angles  
17 between  $20.0^\circ$  and  $26.6^\circ/\langle\bar{1}\bar{1}0\rangle$  is due to the anisotropic lattice dilatation during phase  
18 transformation.

#### 19 **4.2 Variant selection of $\{10\bar{1}2\}$ and $\{11\bar{2}2\}$ twins**

20 During plastic deformation at room temperature,  $\{10\bar{1}2\}$  extension twins and  $\{11\bar{2}2\}$   
21 contraction twins are commonly observed in  $\alpha$ -Ti [19]. OR1 hydride transformation  
22 includes both lattice expansion and shear of  $1/3 \langle 10\bar{1}0 \rangle$  Shockley partial dislocation.  
23 Only dislocation slip is not enough to accommodate such complicated misfit strain, but

1 also twinning is always induced.  $\{10\bar{1}2\}$  and  $\{11\bar{2}2\}$  twins induced by OR1 hydride  
 2 nucleation were observed in our work, which are orientation dependent, as shown in Fig.  
 3 5.  $\{10\bar{1}2\}$  twin prefers the orientation with  $c$ -axis parallel to diffusion direction and  
 4  $\{11\bar{2}2\}$  is easier to be activated in the grain located between the orientations favorable  
 5 for OR1 and OR2.

6 In the current work, we use DGA (deformation gradient accommodation) criterion to  
 7 explore the accommodative twin nucleation which can relax the local distortion at the  
 8 interface of hydrides. The original DGA criterion was employed to predict the secondary  
 9 twinning in magnesium alloys [20] and also extended for the exploration of the  
 10 accommodation between different twin variants in titanium alloys [19]. According to the  
 11 transformation mechanism, the OR1 hydriding frame is set up by:  $\boldsymbol{\eta}$  // gliding direction  
 12 of partial dislocation  $\langle 10\bar{1}0 \rangle$ ,  $\boldsymbol{\gamma}$  // normal of basal plane and  $\boldsymbol{\lambda}$  // the zone axis ( $\boldsymbol{\lambda} = \boldsymbol{\gamma} \times \boldsymbol{\eta}$ ).  
 13 The twin frame is set up by:  $\boldsymbol{n}$  // twinning shear direction,  $\boldsymbol{m}$  // normal of twin habit plane  
 14 and  $\boldsymbol{p}$  // normal of shear plane. The calculated displacement gradient tensors  $\mathbf{D}$  of OR1  
 15 hydride  $\mathbf{D}_H$  and twins  $\mathbf{D}_T$  in their defined reference frames are summarized in Table 3.  
 16 The method of calculating  $\mathbf{D}_H$  and  $\mathbf{D}_T$  can be found in [10] and [20], respectively. The  
 17 different shear values of twin modes are obtained from classical twinning theory [21].

18 At first, the accommodation of twinning on the hydride-induced surface expansion is  
 19 considered as a constraint for the selection between  $\{10\bar{1}2\}$  and  $\{11\bar{2}2\}$  twin modes. The  
 20 contribution of hydrides and twin variants in Grain I and Grain II (see Fig. 5) to the  
 21 expansion along surface normal is evaluated by transforming their displacement gradient  
 22 tensor  $\mathbf{D}$  into sample frame  $\mathbf{D}^s$ :

$$\mathbf{D}^s = \mathbf{R}_{cs}^{-1} \cdot \mathbf{D} \cdot \mathbf{R}_{cs} \quad (2)$$

1 where  $\mathbf{R}_{cs}$  is Bunge rotation matrix [22]. The  $D_{33}^S$  values of B<sub>5</sub> hydride +0.228 in Grain I  
 2 is larger than that of B<sub>2</sub> hydride +0.220 in Grain II. The  $D_{33}^S$  values of  $\{10\bar{1}2\}$  and  $\{11\bar{2}2\}$   
 3 twins in these two grains are summarized in Table 4. The twin variants with larger  $D_{33}^S$   
 4 values have higher capacity to accommodate the expansion along sample surface. As for  
 5 Grain I with *c*-axis close to surface normal, the surface expansion coincides with *c*-axis  
 6 extension, thus all the  $D_{33}^S$  of  $\{10\bar{1}2\}$  tension twin T<sup>I</sup> is positive (bold in Table 4) but  
 7 negative for  $\{11\bar{2}2\}$  twin C<sup>I</sup>, indicating all the six  $\{10\bar{1}2\}$  twin variants are favorable to  
 8 accommodate the surface expansion of B<sub>5</sub> hydride. In contrast, only one  $\{10\bar{1}2\}$  twin  
 9 variant has positive  $D_{33}^S$  in Grain II, while three  $\{11\bar{2}2\}$  twin variants are more preferred  
 10 with larger  $D_{33}^S$  (C<sub>2</sub><sup>I</sup>, C<sub>4</sub><sup>I</sup> and C<sub>5</sub><sup>I</sup>). The basal plane of Grain II is oriented away from  
 11 diffusion surface, thus the surface expansion of B<sub>2</sub> hydride trends to perpendicular to *c*-  
 12 axis equivalent to a *c*-axis compression, which is favorable to be accommodated by  
 13  $\{11\bar{2}2\}$  contraction twinning.

14 A general prediction of orientation for each twin mode is carried out using  $D_{33}^S$  values.  
 15 Fig. 9 plot the maximum  $D_{33}^S$  values associated with respective six  $\{10\bar{1}2\}$  and  $\{11\bar{2}2\}$   
 16 twin variants in the full IPFs with the shown color bar. The crystal orientations with  
 17 maximum  $D_{33}^S$  values around +0.08 are colored by red and less than zero are white. As  
 18 shown in Fig. 9a, the maximum  $D_{33}^S$  (red domain) of  $\{10\bar{1}2\}$  twins focuses on the center  
 19 of IPF, which shows that the  $\{10\bar{1}2\}$  twin is more favorable to accommodate the surface  
 20 expansion in the grain with *c*-axis close to sample normal, coinciding with the  
 21 experimental results in Fig. 5d. In Fig. 9b, the  $D_{33}^S$  value is increase with the larger  
 22 deviation angle of *c*-axis from IPF center, and  $\{11\bar{2}2\}$  twin is preferentially selected in  
 23 the grain with *c*-axis deviated from sample normal. However, no twin was observed in

1 the OR2 favorable orientation with  $c$ -axis fully oriented from **ND**. Thus, as shown in Fig.  
 2 5h, the orientations of grain with  $\{11\bar{2}2\}$  twin-hydride pairs are between the OR1 and  
 3 OR2 favorable positions.

4 To further explore the variant selection among six twin variants of respective  $\{10\bar{1}2\}$   
 5 and  $\{11\bar{2}2\}$  twins, the displacement gradient tensor of OR1 hydride are transformed into  
 6 different twin frames. The coordinate rotation matrix from OR1 hydride system and  
 7 twinning system to crystal frame are shown as follows:

$$\mathbf{R}_{\text{hc}} = \begin{bmatrix} \eta_1 & \eta_2 & \eta_3 \\ \lambda_1 & \lambda_2 & \lambda_3 \\ \gamma_1 & \gamma_2 & \gamma_3 \end{bmatrix} \text{ and } \mathbf{R}_{\text{tc}} = \begin{bmatrix} n_1 & n_2 & n_3 \\ p_1 & p_2 & p_3 \\ m_1 & m_2 & m_3 \end{bmatrix} \quad (3)$$

8 where  $\eta$ - $\lambda$ - $\gamma$  and  $n$ - $m$ - $p$  are OR1 hydriding frame and twinning frames. The transformed  
 9 displacement gradient tensor ( $\mathbf{D}^{\text{H-T}}$ ) from OR1 frame to twinning frame can be expressed  
 10 as:

$$\mathbf{D}^{\text{H-T}} = \mathbf{R}_{\text{tc}} \cdot \mathbf{R}_{\text{hc}}^{-1} \cdot \mathbf{D}_{\text{H}} \cdot \mathbf{R}_{\text{hc}} \cdot \mathbf{R}_{\text{tc}}^{-1} \quad (4)$$

11 The  $D_{13}^{\text{H-T}}$  component of transformed tensor indicates the displacement gradient of  
 12 hydride transformation happens along the shear direction on the twin plane. The twin  
 13 variants with larger  $D_{13}^{\text{H-T}}$  corresponding to higher capability to accommodate the resultant  
 14 strain of hydrides are preferentially selected.

15 The  $D_{13}^{\text{H-T}}$  transformed from activated OR1 hydride variants ( $B_5$  and  $B_2$  in Fig. 5) into  
 16 corresponding twin variants of  $T^I$  and  $C^I$  are shown in Table 5. The bold variants have  
 17 largest  $D_{13}^{\text{H-T}}$  values among six variants of each twin mode and thus are most capable for  
 18 hydride accommodation. In Grain I, the most favorable hydride-twin pair  $B_5$ - $T_2^I$  is  
 19 consistent with the experimental result. Indeed, in the grains with  $\{10\bar{1}2\}$  twin like Grain  
 20 I with  $c$ -axis close to diffusion direction, the accommodative hydride-twin pairs always

1 follow  $B_i-T_{i+3}^I$ . Furthermore, both  $C_1^I$  and  $C_2^I$  have the same largest  $D_{13}^{H-T}$  (+0.080) in  
2 Grain II, while the larger  $D_{33}^S$  of  $C_2^I$  (+0.008) than  $C_1^I$  (0.000) results in the final activation  
3 of  $B_2-C_2^I$  pair. Thus, in the grains with orientation between OR1 and OR2 favorable ones  
4 like Grain II, the  $B_i-C_i^I$  hydride-twin pair can be determined by the combination of surface  
5 expansion and twin shear accommodation.

## 6 **5. Conclusion**

7 The interactions of different hydride variants are for the first time investigated by  
8 section characterization of hydride diffusion layer through EBSD measurement. The  
9 section microstructure of hydrogen diffusion layer is dependent on Ti matrix orientation.  
10 The grains with  $\{10\bar{1}3\}$  and basal plane parallel to the diffusion surface are favorable for  
11 the OR1 hydride layer with one dominant variant and multiple variants, respectively. OR3  
12 hydrides are sometimes stimulated as well near diffusion surface of the grain with former  
13 orientation. The hydride layers in the grains with the orientations of  $\langle 10\bar{1}0 \rangle$  and  
14  $\langle \bar{1}2\bar{1}0 \rangle$  aligned to the diffusion direction mainly encourage OR2 hydrides of three  
15 symmetric variants and two preferential variants, respectively.

16 Two types of deformation twins,  $\{10\bar{1}2\}$  extension and  $\{11\bar{2}2\}$  contraction twins,  
17 are observed at hydride interface to accommodate the misfit strain induced by OR1  
18 hydride nucleation.  $\{10\bar{1}2\}$  twins prefer to be formed in the grains with  $c$ -axis parallel to  
19 the diffusion direction and  $\{11\bar{2}2\}$  twins in the grains located between the orientations  
20 favorable for OR1 and OR2. The orientation dependence of the stimulated twins is due  
21 to the accommodation capacity of  $\{10\bar{1}2\}$  and  $\{11\bar{2}2\}$  twins on the hydride-induced  
22 surface expansion. The further variant selection among the six variants of each twin mode  
23 is determined via displacement gradient accommodation and denoted as  $B_i-T_{i+3}^I$  and  $B_i-$

1  $C_i^I$ . Moreover, the OR2 transformation prefers to take place at grain boundary due to the  
2 larger distortion, while the accumulated prismatic dislocations in the grain interior  
3 provide favorable nucleation positions for intragranular hydride.

#### 4 **Acknowledgements**

5 The authors would like to thank Prof. Eric Fleury for the hydrogen charging device.  
6 The first author Qian Wang is grateful to the China Scholarship Council for the financial  
7 support of her PhD study in France.

#### 8 **References**

- 9 [1] D. Banerjee, J.C. Williams, Perspectives on titanium science and technology, *Acta Mater.* 61 (2013)  
10 844–879.
- 11 [2] I. Guillot, X. Feaugas, M. Clavel, Dislocation-hydride interactions at low plastic strain in titanium,  
12 *Scr. Mater.* 44 (2001) 1011–1017.
- 13 [3] S. Banerjee, P.B.T.-P.M.S. Mukhopadhyay, eds., Chapter 8 - Interstitial Ordering, in: *Phase*  
14 *Transform.*, Pergamon, 2007: pp. 717–781.
- 15 [4] A. San-Martin, F.D. Manchester, The H–Ti (Hydrogen-Titanium) system, *Bull. Alloy Phase*  
16 *Diagrams.* 8 (1987) 30–42.
- 17 [5] E. Conforto, D. Caillard, A fast method for determining favourable orientation relationships and  
18 interface planes: Application to titanium-titanium hydrides transformations, *Acta Mater.* 55 (2007)  
19 785–798.
- 20 [6] A. Bourret, A. Lasalmonie, S. Naka, In-situ high resolution observation of hydride precipitation in  
21 titanium, *Scr. Metall.* 20 (1986) 861–866.
- 22 [7] H. Numakura, M. Koiwa, Hydride precipitation in titanium, *Acta Metall.* 32 (1984) 1799–1807.
- 23 [8] E. Conforto, D. Caillard, Edge-to-edge matching at Ti–TiH interfaces: kinetics of hydride growth  
24 and clustering of precipitates with different orientation relationships, *Solid State Phenom.* 172–174  
25 (2011) 242–247.
- 26 [9] O.T. Woo, G.C. Weatherly, C.E. Coleman, R.W. Gilbert, The precipitation of  $\gamma$ -deuterides  
27 (hydrides) in titanium, *Acta Metall.* 33 (1985) 1897–1906.
- 28 [10] Q. Wang, S. Xu, J.S. Lecomte, C. Schuman, L. Peltier, X. Shen, W. Song, Crystallographic  
29 orientation dependence of hydride precipitation in commercial pure titanium, *Acta Mater.* 183  
30 (2020) 329–339.
- 31 [11] S. Wang, F. Giuliani, T. Ben Britton, Microstructure and formation mechanisms of  $\delta$ -hydrides in  
32 variable grain size Zircaloy-4 studied by electron backscatter diffraction, *Acta Mater.* 169 (2019)  
33 76–87.
- 34 [12] G.J.C Carpenter, The precipitation of  $\gamma$ -hydride plates in zirconium, *Acta Metall.* 29 (1978) 501.
- 35 [13] S. Xu, M. Gong, Y. Jiang, C. Schuman, J.S. Lecomte, J. Wang, Secondary twin variant selection  
36 in four types of double twins in titanium, *Acta Mater.* 152 (2018) 58–76.
- 37 [14] S. Xu, P. Zhou, G. Liu, D. Xiao, M. Gong, J. Wang, Shock-induced two types of {10-12} sequential  
38 twinning in Titanium, *Acta Mater.* 165 (2019) 547–560.
- 39 [15] J.S. Bradbrook, G.W. Lorimer, N. Ridley, The precipitation of zirconium hydride in zirconium and  
40 zircaloy-2, *J. Nucl. Mater.* 42 (1972) 142–160.
- 41 [16] V. Perovic, G.C. Weatherly, C.J. Simpson, Hydride precipitation in  $\alpha/\beta$  zirconium alloys, *Acta*  
42 *Metall.* 31 (1983) 1381–1391.
- 43 [17] Y.B. Chun, M. Battaini, C.H.J. Davies, S.K. Hwang, Distribution Characteristics of In-Grain  
44 Misorientation Axes in Cold-Rolled Commercially Pure Titanium and Their Correlation with

1 Active Slip Modes, *Metall. Mater. Trans. A.* 41 (2010) 3473–3487.  
2 [18] G.C. Weatherly, The precipitation of  $\gamma$ -hydride plates in zirconium, *Acta Metall.* 29 (1981) 501–  
3 512.  
4 [19] S. Xu, M. Gong, C. Schuman, J.-S. Lecomte, X. Xie, J. Wang, Sequential {10-12} twinning  
5 stimulated by other twins in titanium, *Acta Mater.* 132 (2017) 57–68.  
6 [20] É. Martin, L. Capolungo, L. Jiang, J.J. Jonas, Variant selection during secondary twinning in Mg-  
7 3%Al, *Acta Mater.* 58 (2010) 3970–3983.  
8 [21] J.W. Christian, S. Mahajan, Deformation twinning, *Prog. Mater. Sci.* 39 (1995) 1–157.  
9 doi:[https://doi.org/10.1016/0079-6425\(94\)00007-7](https://doi.org/10.1016/0079-6425(94)00007-7).  
10 [22] H.J. Bunge, C. Esling, J. Muller, The influence of crystal and sample symmetries on the orientation  
11 distribution function of the crystallites in polycrystalline materials, *Acta Crystallogr. Sect. A Cryst.*  
12 *Physics, Diffraction, Theor. Gen. Crystallogr.* 37 (1981) 889–899.  
13  
14

1 **Table 1**  
2 Four orientation relationships of  $\alpha$ -Ti /  $\delta$ -hydride (FCC structured) transition.

	Orientation relationship	Interface plane
OR1	$\{0001\} // \{1\bar{1}1\}$ (angle of $4^\circ$ ), $\langle \bar{1}210 \rangle // \langle 110 \rangle$	$\{10\bar{1}3\} // \{1\bar{1}0\}$
OR2	$\{0001\} // \{001\}$ , $\langle \bar{1}210 \rangle // \langle 110 \rangle$	$\{10\bar{1}0\} // \{1\bar{1}0\}$
OR3	$\{10\bar{1}0\} // \{1\bar{1}1\}$ , $\langle \bar{1}210 \rangle // \langle 110 \rangle$	$\{0001\} // \{1\bar{1}2\}$
OR4	$\{\bar{1}011\} // \{001\}$ , $\langle \bar{1}210 \rangle // \langle 110 \rangle$	$\{10\bar{1}1\} // \{1\bar{1}\bar{1}\}$

3  
4 **Table 2**  
5 Variants of hydride and twin

	Variant 1	Variant 2	Variant 3	Variant 4	Variant 5	Variant 6
OR1 hydride ( $B_i$ )	$(10\bar{1}3)[10\bar{1}0]$	$(01\bar{1}3)[01\bar{1}0]$	$(\bar{1}103)[\bar{1}100]$	$(\bar{1}013)[\bar{1}010]$	$(0\bar{1}13)[0\bar{1}10]$	$(1\bar{1}03)[1\bar{1}00]$
OR2 hydride ( $P_i$ )	$(10\bar{1}0)$	$(01\bar{1}0)$	$(\bar{1}100)$			
$\{10\bar{1}2\}$ twin ( $T_i^I$ )	$(10\bar{1}2)[\bar{1}011]$	$(01\bar{1}2)[0\bar{1}11]$	$(\bar{1}102)[\bar{1}\bar{1}01]$	$(\bar{1}012)[10\bar{1}1]$	$(0\bar{1}12)[01\bar{1}1]$	$(1\bar{1}02)[\bar{1}101]$
$\{11\bar{2}2\}$ twin ( $C_i^I$ )	$(11\bar{2}2)[11\bar{2}\bar{3}]$	$(\bar{1}2\bar{1}2)[\bar{1}2\bar{1}\bar{3}]$	$(\bar{2}112)[\bar{2}11\bar{3}]$	$(\bar{1}\bar{1}22)[\bar{1}\bar{1}2\bar{3}]$	$(1\bar{2}12)[1\bar{2}1\bar{3}]$	$(2\bar{1}\bar{1}2)[2\bar{1}\bar{1}\bar{3}]$

6  
7 **Table 3**  
8 Displacement gradient tensor of OR1 hydriding and twinning in  $\alpha$ -titanium ( $c/a=1.587$ ).

OR1 hydride ( $D_H$ )	Twinning ( $D_T$ )	
	$T^I$	$C^I$
	$\{10\bar{1}2\} \langle \bar{1}011 \rangle$	$\{11\bar{2}2\} \langle 11\bar{2}\bar{3} \rangle$
$\begin{bmatrix} 0.055 & 0 & 0.384 \\ 0 & 0.055 & 0 \\ 0 & 0 & 0.086 \end{bmatrix}$	$\begin{bmatrix} 0 & 0 & 0.173 \\ 0 & 0 & 0 \\ 0 & 0 & 0 \end{bmatrix}$	$\begin{bmatrix} 0 & 0 & 0.218 \\ 0 & 0 & 0 \\ 0 & 0 & 0 \end{bmatrix}$

9  
10 **Table 4**  
11 The values  $D_{33}^S$  obtained by transforming displacement gradient tensors from  $\{10\bar{1}2\}$  and  $\{11\bar{2}2\}$   
12 twinning frames into sample frame. The bold variants are more favorable.

	Variant 1	Variant 2	Variant 3	Variant 4	Variant 5	Variant 6
$B_5$ (Grain I)	$T_1^I + \mathbf{0.071}$	$T_2^I + \mathbf{0.063}$	$T_3^I + \mathbf{0.071}$	$T_4^I + \mathbf{0.066}$	$T_5^I + \mathbf{0.052}$	$T_6^I + \mathbf{0.065}$
	$C_1^I - 0.038$	$C_2^I - 0.038$	$C_3^I - 0.081$	$C_4^I - 0.100$	$C_5^I - 0.100$	$C_6^I - 0.082$
$B_2$ (Grain II)	$T_1^I + \mathbf{0.004}$	$T_2^I - 0.056$	$T_3^I - 0.008$	$T_4^I - 0.009$	$T_5^I - 0.044$	$T_6^I - 0.001$
	$C_1^I 0.000$	$C_2^I + \mathbf{0.008}$	$C_3^I - 0.024$	$C_4^I + \mathbf{0.063}$	$C_5^I + \mathbf{0.078}$	$C_6^I - 0.017$

13  
14 **Table 5**  
15 The values  $D_{13}^{H-T}$  obtained by transforming displacement gradient tensors from hydriding frame into the  
16 twinning frames. The bold variants are more favorable.

	Variant 1	Variant 2	Variant 3	Variant 4	Variant 5	Variant 6
B <sub>5</sub> (Grain I)	T <sub>1</sub> <sup>I</sup> +0.120	<b>T<sub>2</sub><sup>I</sup> +0.224</b>	T <sub>3</sub> <sup>I</sup> +0.120	T <sub>4</sub> <sup>I</sup> +0.089	T <sub>5</sub> <sup>I</sup> -0.193	T <sub>6</sub> <sup>I</sup> -0.089
B <sub>2</sub> (Grain II)	<b>C<sub>1</sub><sup>I</sup> +0.080</b>	<b>C<sub>2</sub><sup>I</sup> +0.080</b>	C <sub>3</sub> <sup>I</sup> -0.014	C <sub>4</sub> <sup>I</sup> -0.108	C <sub>5</sub> <sup>I</sup> -0.108	C <sub>6</sub> <sup>I</sup> -0.014

1  
2

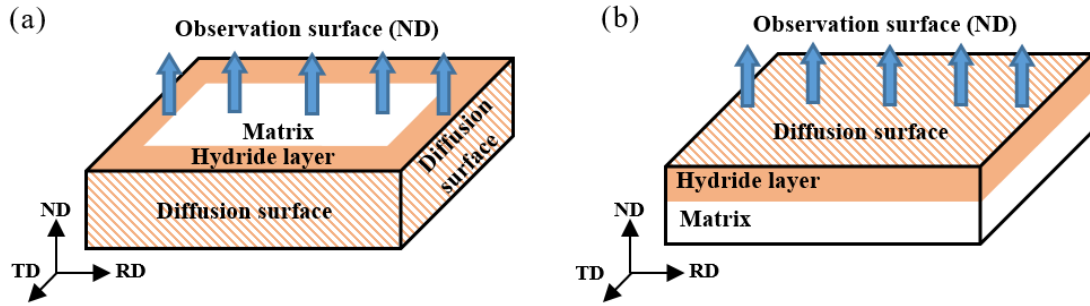


**Fig. 1.** Illustration of sample preparation (a) Sample A used to observe section microstructure of hydride layer and (b) Sample B for characterization of hydride induced plastic deformation.

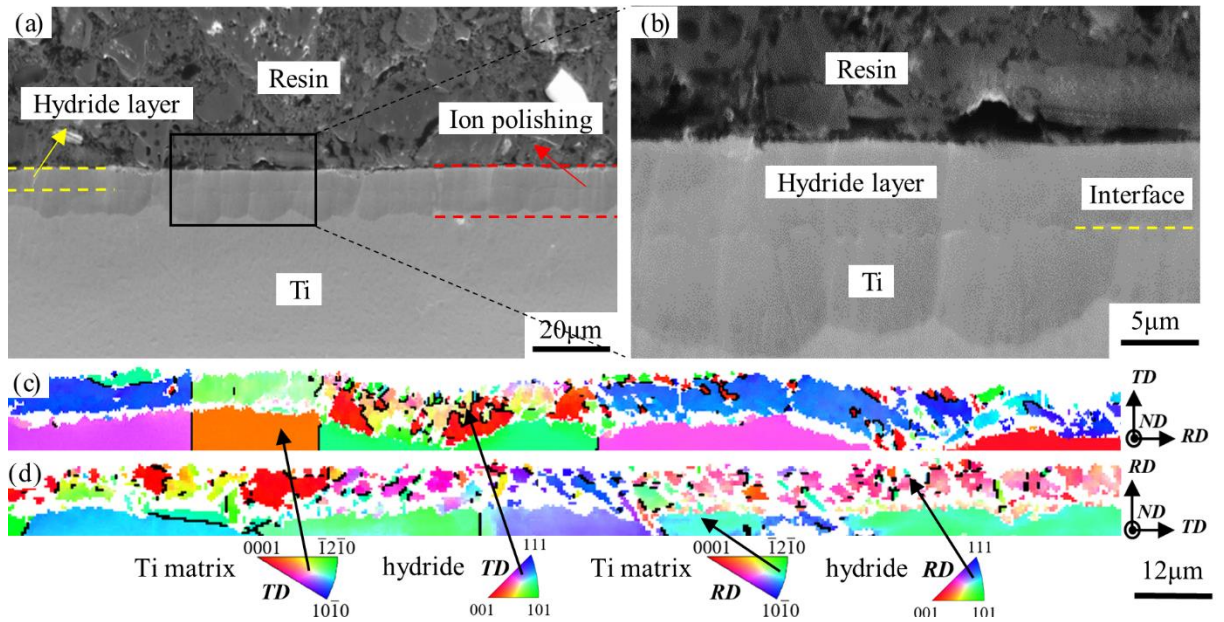
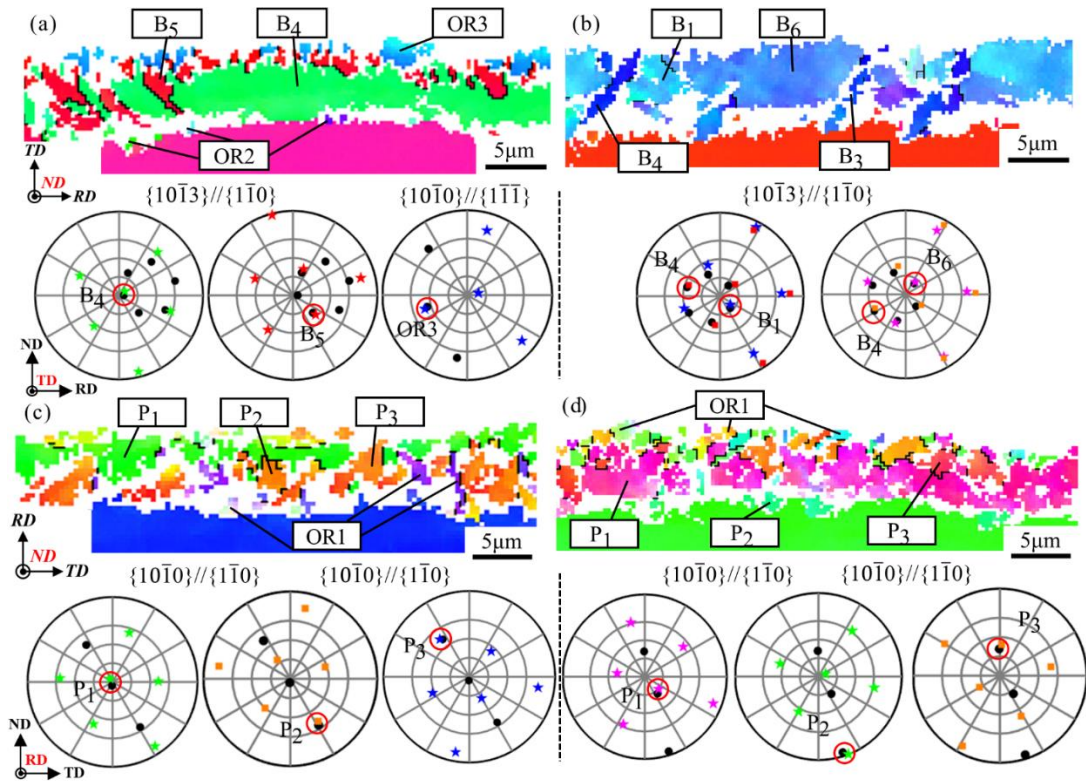
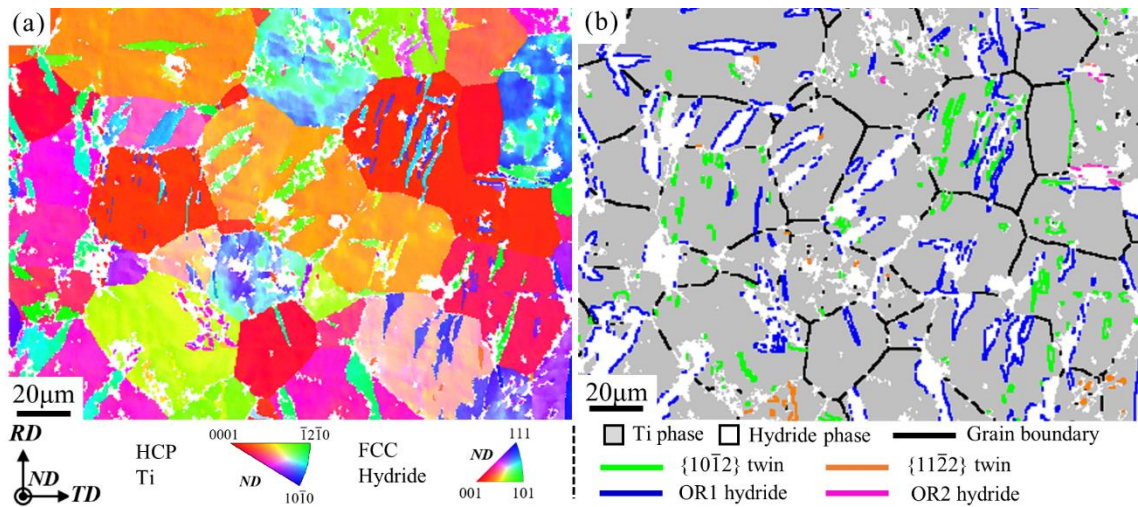


**Fig. 2.** (a) SEI showing section microstructure of hydride layer. (b) The higher-magnification SEM of the area in the black box. (c) TD-IPF maps of hydride layer formed on TD surface. (d) RD-IPF maps of hydride layer formed on RD surface. Grain boundaries are indicated by black lines in the IPF maps.



1  
2  
3 **Fig. 3.** IPF maps of hydride layer and corresponding pole figures of hydride variants in (a) Grain 1, Euler  
4 angle: 37.9°, 82.5°, 13.3°, (b) Grain 2, Euler angle: 166.2°, 87.1°, 26.3°, (c) Grain 3, Euler angle: 101.1°,  
5 73.3°, 22.9° and (d) Grain 4, Euler angle: 86.7°, 57.1°, 5.2°. The IPF maps are colored with hydrogen  
6 diffusion direction. Grain boundaries are indicated by black line. The black dots in pole figures represent  
7 the  $\{10\bar{1}3\}$  or  $\{10\bar{1}0\}$  interface planes of Ti matrix and the color dots refer to the  $\{1\bar{1}0\}$  or  $\{1\bar{1}\bar{1}\}$  planes of  
8 hydrides.  
9  
10  
11



12  
13  
14 **Fig. 4.** (a) ND-IPF map of Ti matrix and hydride precipitates with corresponding color code. (b) Phase map  
15 with Ti matrix in silver and white hydride. The hydride and twin boundaries are highlighted by color lines:  
16  $\{10\bar{1}2\}$  extension twins (green),  $\{11\bar{2}2\}$  contraction twins (orange), interface planes of OR1 hydrides (blue)  
17 and OR2 hydrides (pink). Black lines refer to grain boundaries ( $>5^\circ$ ).

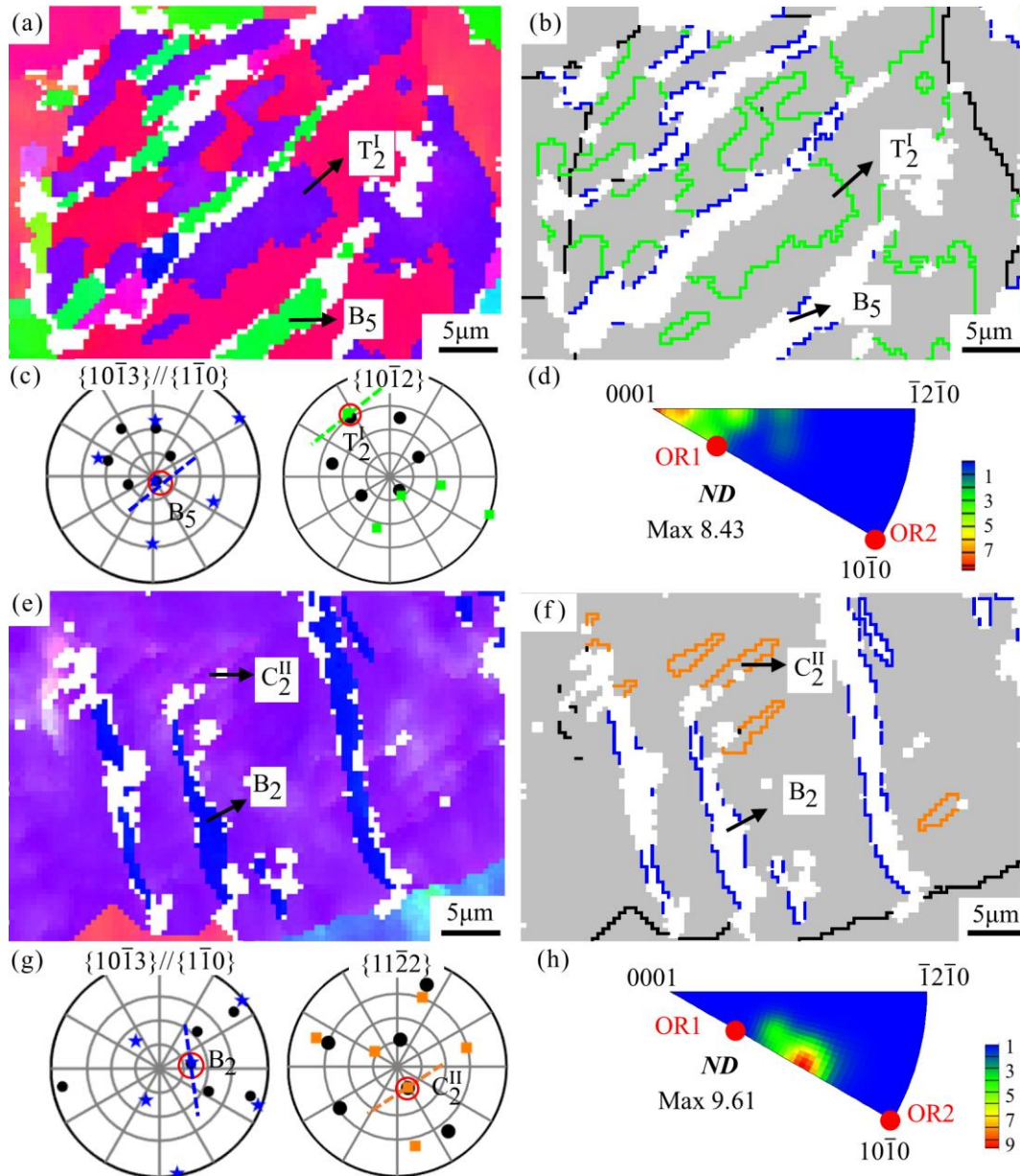


**Fig. 5.** (a) and (e) ND-IPF map of Grain I (Euler angles: 33.2°, 155.5°, 29.2°) containing  $\{10\bar{1}2\}$  twin-hydrate pairs and Grain II (Euler angles: 100.2°, 62.6°, 25.1°) containing  $\{11\bar{2}2\}$  twin-hydrate pairs. (b) and (f) Phase maps of Grain I and Grain II. The color code for the EBSD maps is the same as Fig. 4. (c) and (g) Pole figures of  $\{10\bar{1}3\}$ ,  $\{10\bar{1}2\}$  and  $\{11\bar{2}2\}$  planes. The black dots represent the planes of Ti matrix and the color ones are the planes of hydrides or twins. The dotted lines represent the traces of corresponding interface planes of hydrides. (d) and (h) IPF contouring maps of all the grains with respective  $\{10\bar{1}2\}$  and  $\{11\bar{2}2\}$  twin-hydrate pairs. The OR1 and OR2 favorable orientations are indicated by red points.

1  
 2  
 3  
 4  
 5  
 6  
 7  
 8  
 9  
 10  
 11  
 12  
 13  
 14  
 15  
 16

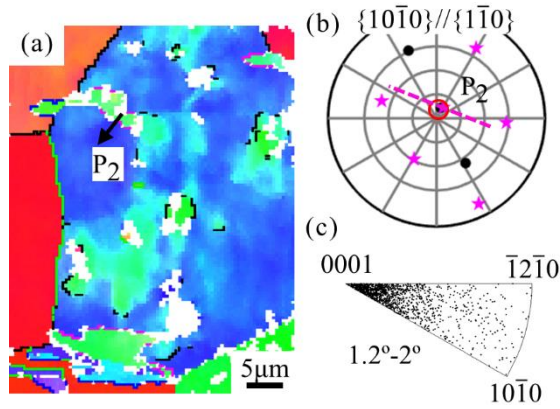


**Fig. 6.** (a) IPF map of Grain III (Euler angles:  $116.0^\circ$ ,  $98.2^\circ$ ,  $21.1^\circ$ ) containing OR2 hydrides. The color code for the IPF maps is the same as Fig. 4. (b)  $\{10\bar{1}0\}$  pole figure, the black dots represent the planes of Ti matrix and the color ones represent the hydride planes. The dotted lines represent the traces of corresponding interface planes of hydrides. (c) IGMA distributions obtained from the misorientation angles of Grain III.

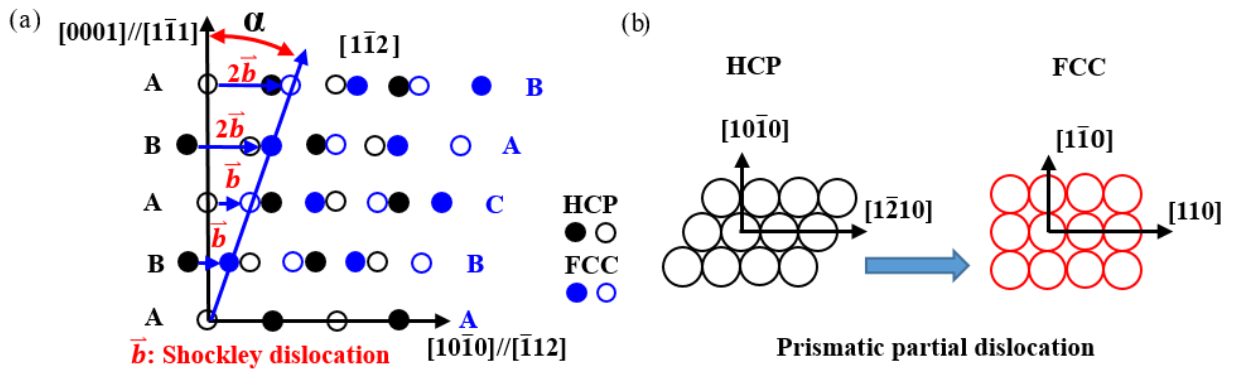
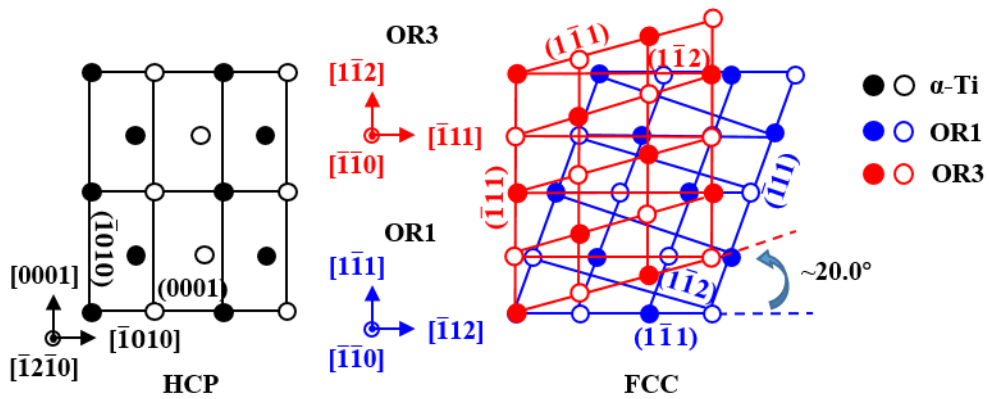
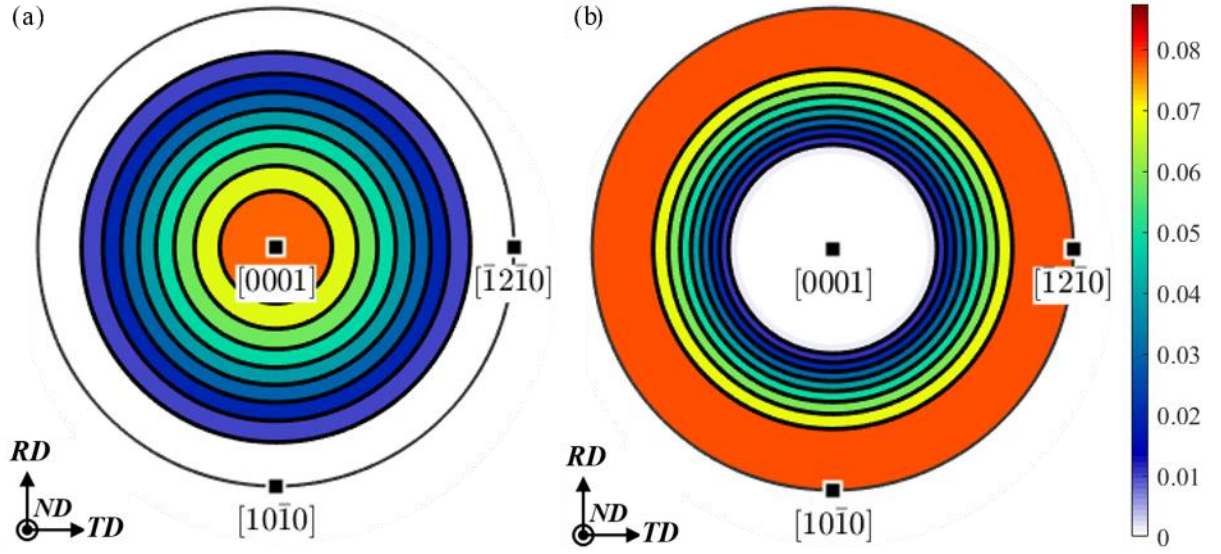


**Fig. 7.** Illustration of HCP-FCC structure transformation of (a) OR1 and (b) OR2 hydride. The filled and open circles are in the different atom layers.



1 **Fig. 8.** The relationship of HCP-FCC structure transformations between OR1 and OR3 hydrides. The  
 2 filled and open circles are in the different atom layers.

3



4

5 **Fig. 9.** Full inverse pole figure of  $D_{33}^S$  value for (a) six  $\{10\bar{1}2\}$  twin variants and (b)  $\{11\bar{2}2\}$  twin  
 6 variants

7

8